

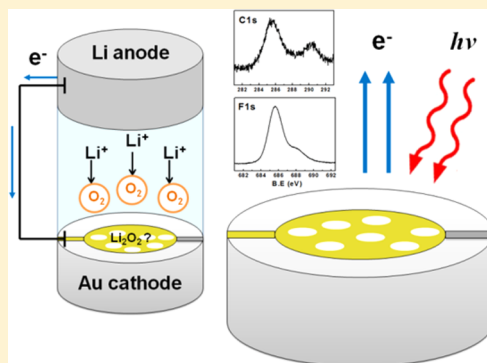
# Surface Study of Lithium–Air Battery Oxygen Cathodes in Different Solvent–Electrolyte pairs

F. Marchini, S. Herrera, W. Torres, A.Y. Tesio, F.J. Williams, and E.J. Calvo\*

INQUIMAE, Facultad de Ciencias Exactas y Naturales, Pabellón 2, Ciudad Universitaria, AR-1428 Buenos Aires, Argentina

## Supporting Information

**ABSTRACT:** The  $O_2/Li_2O_2$  electrode reaction has been studied on low surface area Au electrodes in three solvent–electrolyte pairs (0.1 M  $LiPF_6/DMSO$ ,  $LiPF_6/ACN$ , and  $LiBF_4/ACN$ ) using an electrochemical cell coupled to UHV XPS spectrometer, EQCM, AFM, and DEMS. The XPS spectra of the surfaces after treatment at selected electrode potentials for the  $O_2$  reduction and reoxidation of the surface show the presence of C and S from solvent decomposition and of F and P from electrolyte decomposition. Furthermore, Li 1s and O 1s peaks due to  $Li_2O_2$  and decomposition products such as carbonate, organics, LiF, high oxidation sulfur, and phosphorus compounds were also observed. Using ACN instead of DMSO results in less solvent decomposition, whereas using  $LiBF_4$  results in less electrolyte decomposition. XPS, AFM, and EQCM show that  $O_2$  reduction products removal only takes place at very high overpotentials. In agreement with XPS which shows removal of carbonate surface species, DEMS confirms evolution of  $CO_2$  and consumption of  $O_2$  at 4.5 V, but LiF cannot be removed completely in a round trip of the Li– $O_2$  battery cathode.



## INTRODUCTION

The rechargeable lithium–air battery exhibits a very large theoretical energy density that can compete with fossil fuels for electric vehicle applications with extended millage range.<sup>1–5</sup> In the non aqueous Li–air battery during discharge a Li anode dissolves in non aqueous electrolyte and the resulting  $Li^+$  ions react with  $O_2$  reduction reaction (ORR) products to form insoluble lithium peroxide ( $Li_2O_2$ ) at a porous carbon cathode.<sup>6,7</sup> Among non aqueous solvents, DMSO with a very large dipolar moment ( $\mu = 4.3$  D) has been used in Li– $O_2$  cathodes<sup>8–10</sup> and Bruce reported rechargeability of this battery with 95% capacity retention in 100 cycles using dimethyl sulfoxide (DMSO) electrolyte and porous Au electrode. However, there is a controversy on the stability of insoluble  $Li_2O_2$  produced during  $O_2$  discharge as shown by an iodometric titration of  $Li_2O_2$  to determine the quantitative formation and oxidation of lithium peroxide in the bulk battery material. McCloskey et al.<sup>11</sup> have shown that the balance of oxygen consumed in the ORR and produced in the oxygen evolution reaction (OER) during charging is always less than 0.9. The authors concluded that while the ORR is a 2-electron process yielding  $Li_2O_2$ , further heterogeneous chemical reaction of the solid peroxide with the electrolyte or the carbon cathode decreased the amount of peroxide on the surface so that the outermost surface of  $Li_2O_2$  can react chemically with the electrolyte decomposing the solvent and/or the electrolyte.<sup>12</sup> Differential electrochemical mass spectrometry (DEMS) studies by different groups and different solvent–electrolyte pairs have shown that the moles of  $O_2$  measured upon charge is significantly less than expected for complete peroxide formation

and decomposition in agreement with fading capacity observed during cycling.<sup>12–14</sup> Bondue et al.<sup>15</sup> have recently reported DEMS experiments under ambient air with humidity and  $CO_2$  present with Au sputtered Teflon membrane gas diffusion electrode in DMSO and  $LiClO_4$  which yielded true Coulombic efficiencies below 100%.

In parallel, there has been recent evidence of DMSO decomposition mainly to carbonate species when it is in contact with solid  $Li_2O_2$  and other side products such as  $LiOH$ , dimethyl sulfone,  $Li_2SO_3$  and  $Li_2SO_4$ , have been detected.<sup>12,16</sup> XPS studies have shown that DMSO decomposes at the  $Li_2O_2$  solid/liquid solvent interface while acetonitrile showed no evidence of degradation.<sup>16</sup> In addition  $LiBF_4$ ,  $LiBOB$ , and  $LiTFSI$  have shown good stability in the presence of  $Li_2O_2$  in several solvents,  $LiPF_6$  and  $LiClO_4$  were reported to react with  $Li_2O_2$  to generate  $OPF_2OLi$  and  $LiF$ .<sup>12,16,17</sup> Aurbach has recently confirmed with EQCM simultaneous to cyclic voltammetry of oxygen reduction on Au and spectroscopy studies on carbon microfibers the instability of DMSO lithium electrolyte for Li–air batteries.<sup>18–21</sup>

Recent results with rotating ring-disk electrode (RRDE) and electrochemical quartz crystal microbalance have shown the stability of lithium superoxide in DMSO electrolyte and the codeposition of the solvent during the formation of  $Li_2O_2$  deposit on the electrode surface.<sup>19–21</sup>

Received: June 10, 2015

Revised: July 28, 2015

Two parallel mechanisms are now accepted for the O<sub>2</sub> electroreduction in lithium electrolytes with high donor-number (DN) solvents, like DMSO, with strong solvation of the Li<sup>+</sup> ion.<sup>22–26</sup> (i) a surface superoxide disproportionation or two consecutive electron ORR steps and (ii) a solution phase mechanism with soluble lithium peroxide disproportionation and precipitation forming large toroidal Li<sub>2</sub>O<sub>2</sub> particles. The relevance of either mechanism would also depend on the current density<sup>22</sup> and traces of water present in the electrolyte.<sup>27</sup>

Our previous “in situ” FTIR studies of LiPF<sub>6</sub> in DMSO at low specific area gold electrodes have failed to detect degradation products of the solvent but demonstrated that DMSO is electrochemically oxidized to dimethyl sulfone above 4.3 V.<sup>28</sup> while most studies have been conducted with large surface area electrodes or bulk battery material, in the present communication we explore the composition at the electrode/electrolyte interface by XPS, EQCM, AFM, and DEMS where the high surface selectivity of these techniques determines a very high area to volume ratio explored. We have studied both, ORR and OER processes in O<sub>2</sub> saturated solutions of three different solvent–electrolyte pairs, that is, 0.1 M LiPF<sub>6</sub>/DMSO, LiPF<sub>6</sub>/ACN, and LiBF<sub>4</sub>/ACN unveiling the underlying processes behind the battery O<sub>2</sub> cathode capacity fading.

## EXPERIMENTAL SECTION

XPS measurements were performed using an SPECS GmbH ultrahigh vacuum (UHV) chamber equipped with a transfer system built in our laboratory that allows easy and rapid controlled transfer of the sample between the UHV environment and the liquid non aqueous electrolyte containing either Ar or O<sub>2</sub> gas at atmospheric pressure. The EC-UHV transfer system has been described elsewhere<sup>29</sup> and details can be found in the Supporting Information. In XPS experiments, the high purity polycrystalline gold sample was Ar<sup>+</sup> sputtered and annealed in subsequent cycles until no impurities were detected by XPS. The spectroscopically clean Au sample was then transferred from the UHV environment to the preparation chamber without exposure to the laboratory atmosphere. Electrochemical measurements at the EC-UHV system were carried out using an operational amplifier potentiostat (TEQ Argentina). A standard three-electrode electrochemical cell was employed with a platinum sheet counter electrode and a LiMn<sub>2</sub>O<sub>4</sub>/Li<sub>2</sub>Mn<sub>2</sub>O<sub>4</sub> reference electrode in the same Li electrolyte.<sup>30</sup> The reference electrode potential measured in a glovebox with respect to a lithium foil in 0.1 M LiPF<sub>6</sub>/DMSO was 3.25 and 2.90 V in 0.1 M LiPF<sub>6</sub>/CH<sub>3</sub>CN respectively. Herein all potentials are quoted with respect to the Li/Li<sup>+</sup> scale in the respective solvent. The electrolyte was saturated in Ar or O<sub>2</sub> forming a meniscus with the Au working electrode. Chronoamperometry was performed at selected potentials during 180 s, after which the electrolyte was extracted with a syringe and the electrode was extensively rinsed with pure dry solvent and dried under a constant flow of Argon in the Teflon cell connected to the UHV system. XPS spectra were acquired on grounded conducting substrate at a constant pass energy of 20 eV using a Mg Kα (1253.6 eV) source operated at 12.5 kV and 20 mA at a detection angle of 30° with respect to the sample normal. Atomic ratios were calculated from the integrated intensities of core levels after instrumental and photoionization cross-section corrections.

AFM images of flamed annealed Arandee Robax Au surfaces were acquired with an Agilent 5500 Atomic force microscope (Agilent Technologies) in contact with dry air before and after the electrochemical experiment.<sup>31</sup> A three electrode EC-AFM electrochemical cell was built using Teflon and a Kalrez O-ring pressed onto the sample with a 0.64 cm<sup>2</sup> area. The auxiliary electrode was a Pt gauze (Good-fellow PT008710/43) and the reference electrode was a Pt wire coated with a LiMn<sub>2</sub>O<sub>4</sub>/Li<sub>2</sub>Mn<sub>2</sub>O<sub>4</sub> in the same Li<sup>+</sup> electrolyte. The cell was contained in a glass cylinder environmental chamber filled with dry oxygen. Electrochemical cyclic voltammetry and chronoamper-

ometry experiments were carried out with a potentiostat/galvanostat coupled with the AFM (EC-AFM, Agilent 5500 AFM/SPM).

The electrode surfaces were scanned by AFM using and insulating triangular Si tip Point-Probe Plus Non-Contact/Soft Tapping Mode (radius <10 nm force constant 48 N·m<sup>-1</sup>, resonance frequency 157.85 kHz) using non contact mode. In a typical experiment after the electrochemical treatment the electrode surface was rinsed with 10 aliquots of 100 μL of non aqueous solvent and dried under Ar. Image analysis was performed with Gwyddion 2.33 software (<http://Gwyddion.net/>).

Anhydrous DMSO (≥99.9%) and acetonitrile and lithium hexafluoro phosphate battery grade, ≥ 99.99% trace metals basis were purchased from Aldrich and stored in the argon-filled MBRAUN glovebox with a water content below 1 ppm and oxygen content below 0.1 ppm.

The water content of the solvents was determined using the Karl Fisher 831 KF Coulometer (Metrohm) and resulted less than 30 ppm. The electrolyte solutions prepared in the glovebox were transferred by syringes to the electrochemical cell without contact with the atmosphere.

The EQCM experiments have been described elsewhere,<sup>32</sup> in brief: A complex voltage divider reported elsewhere was used to measure the resonance frequency and both components of the quartz crystal modified Butterworth–Van Dyke (lumped-element BVD) equivalent circuit. This device operates by applying to the quartz crystal a 10 MHz sinusoidal voltage (5 mV peak-to-peak) generated by a voltage-controlled oscillator (VCO) connected to the D/A output of a data acquisition system. Both input (V<sub>i</sub>) and output (V<sub>o</sub>) ac voltage moduli were amplified and rectified, and the resulting signals were measured with an A/D converter under computer control. The ratio of the circuit transfer function modulus, that is, |V<sub>o</sub>/V<sub>i</sub>| as a function of the VCO output signal frequency was fitted to the nonlinear analytical equation of the BVD transfer function, and the equivalent circuit elements L, R, C<sub>0</sub>, and C were obtained. For low crystal load by the surface deposit (Z<sub>L</sub> ≪ Z<sub>Q</sub>) a lumped element circuit can be approximated and the shift in the quartz impedance due to the ORR products deposit can be written: ΔZ = ΔR + jΔ(ωL), where ΔR and Δ(ωL) are the real and imaginary parts of the impedance shift with respect to the initial quartz crystal condition. Thus, equivalent to the Sauerbrey equation that relates the resonant frequency with the areal mass of deposit:

$$\Delta(\omega L) = -\frac{\pi Z_Q \Delta f}{f_0} = \frac{2\pi Z_Q \Delta m}{\sqrt{(\rho_Q \mu_Q) A}}$$

Where Δf is the measured frequency shift, f<sub>0</sub> the resonant frequency, Δm the mass loading, A the piezoelectrically active area, the quartz density ρ<sub>Q</sub> = 2.648 g·cm<sup>-3</sup>, the shear modulus of AT-cut quartz μ<sub>Q</sub> = 2.947 × 10<sup>11</sup> dyn cm<sup>-2</sup> and the quartz crystal impedance, Z<sub>q</sub> ~ 535 000 Ω. Therefore, the quartz resonator resonance frequency responds both to changes in the inertial mass as well as surface deposit viscoelastic changes and liquid electrolyte. For acoustically thin films (ΔR ≪ Δ(ωL)) changes in resonant frequency or Δ(ωL) can be related to changes in the mass per unit area deposited on the Au coated quartz crystal. Calibration of the EQCM was done with electrochemical deposition of silver and the operational conversion factor used is 5.3 × 10<sup>-8</sup> g·Ω<sup>-1</sup>·cm<sup>-2</sup>.

Differential electrochemical mass spectrometry (DEMS) was accomplished using a Pfeiffer vacuum Omnistar GSD 320 gas analysis system with a quadrupole mass spectrometer QGM 220 (mass range 1–200 amu) with ion gastight ion source, yttriated iridium-filament with secondary electron multiplier C-SEM and Faraday detectors. The DEMS cell setup was a modification of the design pioneered by Baltruschat et al.<sup>33,34</sup> and consisted of a stainless steel base with a PTFE body. A gold sputtered PTFE membrane gas diffusion electrode (200 μm thick and 0.1 μm pore diameter T01047WPH Microclar Teflon) with 0.50 cm<sup>2</sup> geometric electroactive area located at the bottom of the cell. The Au sputtered membrane was mechanically supported on a porous stainless steel frit. Surface tension of the solvent DMSO (43.5 mN m<sup>-1</sup>) prevents penetration in the capillary porous

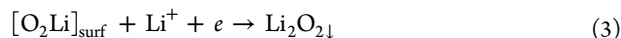
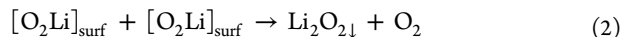
structure of the PTFE membrane.<sup>35,36</sup> The electrolyte-vacuum interface was connected to the gas analyzer by 1/16" ss tubing through a Varian precision needle valve adjusted at  $2 \times 10^{-6}$  mbar. A nonaqueous  $\text{LiMn}_2\text{O}_4/\text{LiMn}_2\text{O}_4$ <sup>30</sup> reference electrode in the same electrolyte was used in a fritted glass compartment and a 1  $\text{cm}^2$  platinum gauze (Johnson Matthey) was employed as counter electrode. The flow system consisted of a Cole-Parmer Co. micropump to circulate the non aqueous electrolyte through the DEMS cell in an airtight system.

## RESULTS AND DISCUSSION

In non aqueous electrolyte with large cations, that is, TBAP,  $\text{O}_2/\text{O}_2^-$  is an outer sphere reversible redox couple.<sup>37</sup> In lithium containing electrolyte, on the other hand, there is a fundamental difference since the reaction product,  $\text{Li}_2\text{O}_2$ , is insoluble. Therefore, one expects a strong influence of the electrode material, electrolyte, solvent (i.e., donor number DN) and experimental conditions such as current density, sweep rate, anodic limit, trace amount of water, etc.

We analyze the ORR on low surface area Au in contact with  $\text{O}_2$  saturated DMSO containing 0.1 M  $\text{LiPF}_6$ . As shown in Figure 1 the reaction takes place at potentials below 2.75 V and shows a characteristic peak at 2.5 V.<sup>10,38</sup> Simultaneous gravimetry with the EQCM depicts the  $\Delta m/A$  increase during

ORR in the forward potential scan and at the beginning of the backward scan due to a continuous deposit of  $\text{Li}_2\text{O}_2$  on the surface as expected from the surface reactions:



Or the solution pathway:<sup>24,40–42</sup>



where subscripts surf and soln denote surface and solution species, respectively.

In Figure 1 we have indicated with dotted line three potentials of interest: 2.05 V where ORR is expected to yield insoluble  $\text{Li}_2\text{O}_2$ , 3.35 V where oxidation of ORR products starts, and 4.55 V where surface reoxidation is almost complete.

Notice the differences in the mass-potential curves at 2 and 20  $\text{mV}\cdot\text{s}^{-1}$  respectively in Figure 1A and B. At low sweep rate the deposition time is longer and a larger mass is observed as compared to the fastest experiment in Figure 1B. Also, the mass increase at 2.44 V is delayed with respect to the cathodic current due to the formation of soluble  $\text{LiO}_2$  as detected with the rotating ring disk electrode (RRDE)<sup>40</sup> which favors the solution pathway with massive deposition of large  $\text{Li}_2\text{O}_2$  particles.<sup>24</sup>

Examination of current traces in Figure 1 suggests that the Au surface is not passivated since the current in the back scan does not drop to zero consistent with the formation of large particles with uncovered surface areas rather than a thin uniform film. The lack of passivation could be caused by traces of water in DMSO solution (157 ppm at the end of that experiment) inducing a solution phase ORR mechanism as demonstrated by the IBM group to enhance the formation of large  $\text{Li}_2\text{O}_2$  particles.<sup>23</sup> Different authors reported for the same system passive<sup>39,43</sup> and non passive<sup>44,45</sup> surface deposits depending on the experimental conditions.

In a recent study we have proposed that DMSO would be codeposited with the lithium oxides from the charge to mass ratio found with the EQCM and thus the solvent at the surface could react with solid  $\text{Li}_2\text{O}_2$  at the solid–liquid interface.<sup>46</sup> From the data in Figure 1 values of mass per electron (mpe) in large excess with respect to those expected from eqs 1–4 have been observed, namely 622 g/mol (Figure 1a) and 402 g/mol (Figure 1b) respectively. This experimental evidence strongly suggests the incorporation of solvent or solvent decomposition products in the surface deposit with molar masses well above those of the lithium oxides.

The reversible potential for the  $\text{O}_2/\text{Li}_2\text{O}_2$  electrode is 2.96 V; however, the oxygen cathodes in lithium electrolyte show a very high anodic overpotential during recharge. The removal of oxygen reduction products from the electrode surface in cyclic voltammetry experiments at different anodic potential windows has shown that only when 4.7 V anodic limit is reached, a second potential sweep in the ORR region shows complete recovery of both the ORR current at a disc and superoxide oxidation current at a Au ring electrode of a RRDE.<sup>38,40</sup>

Inspection of Figure 1 shows that during the oxidation cycle a very modest mass decrease is observed above the reversible  $\text{O}_2/\text{Li}_2\text{O}_2$  electrode potential (2.96 V) and, depending on the time scale of the experiment (2 or 20  $\text{mV}\cdot\text{s}^{-1}$ ), only an almost total mass recovery is observed above 4.5 V where DMSO is

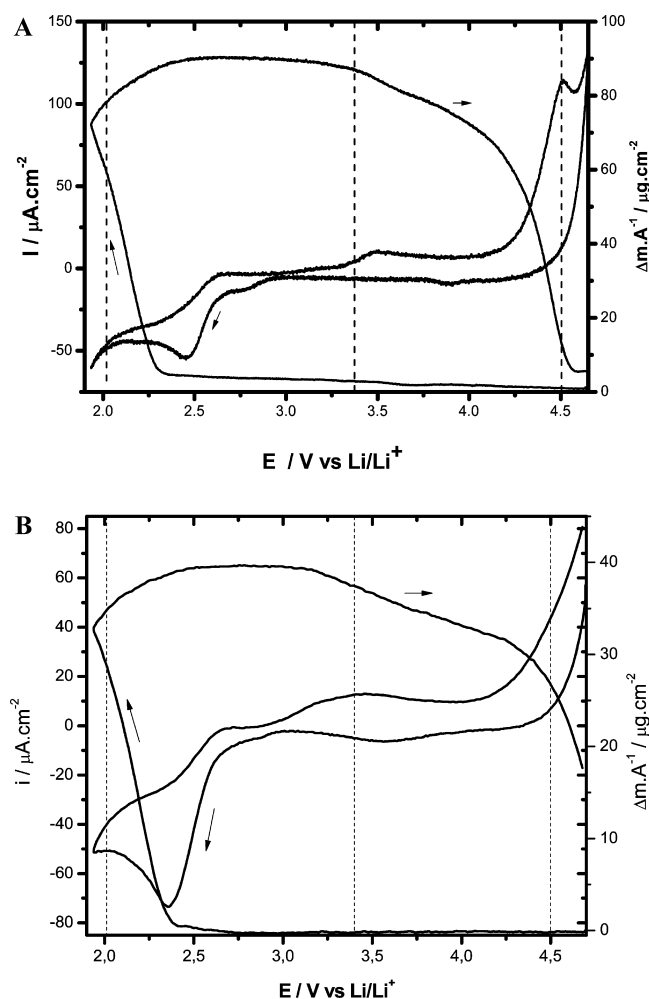


**Figure 1.** Cyclic voltammetry and simultaneous EQCM mass per unit area for the  $\text{O}_2$  reduction on Au coated quartz in 0.1 M  $\text{LiPF}_6$   $\text{O}_2$  saturated DMSO. Sweep rate (A) 2  $\text{mV}\cdot\text{s}^{-1}$ , (B) 20  $\text{mV}\cdot\text{s}^{-1}$  (157 ppm of  $\text{H}_2\text{O}$  after measurement).

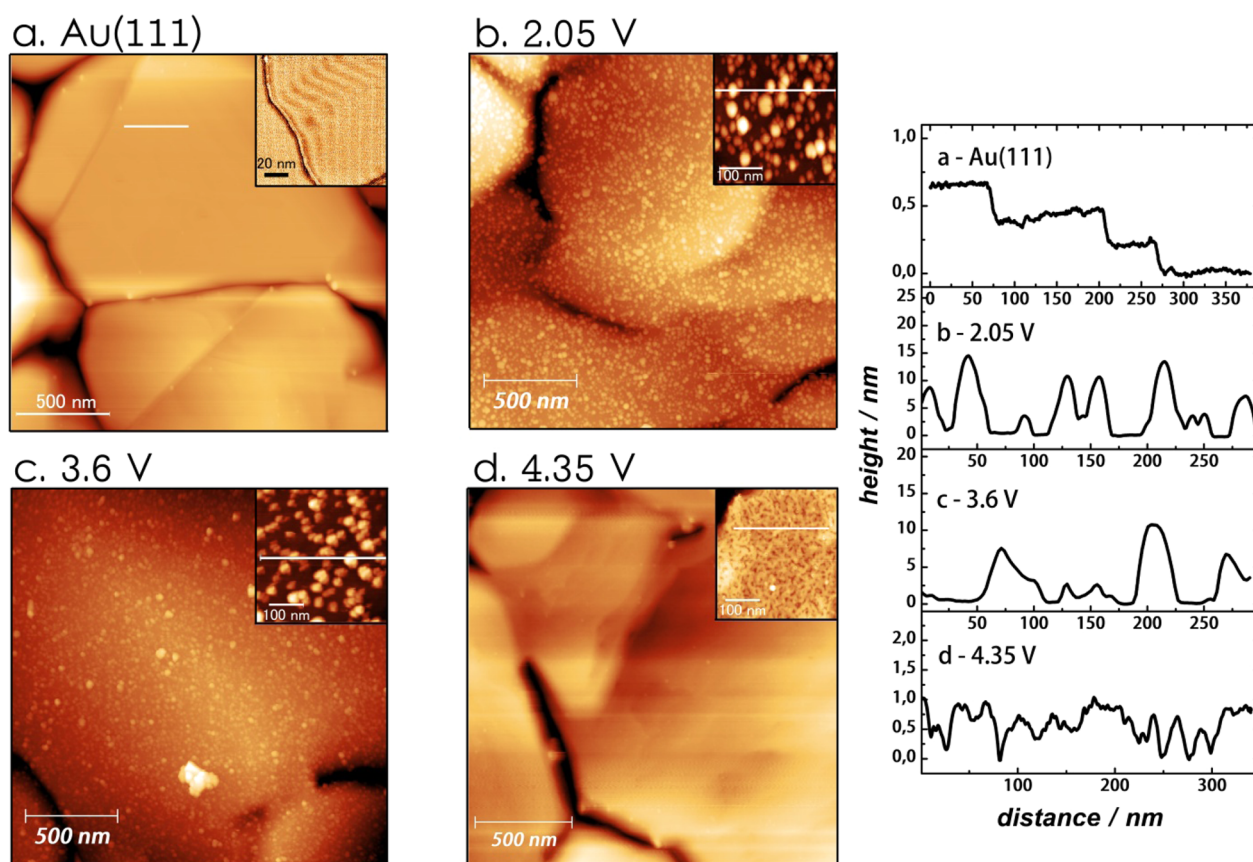


**Figure 2.** Ex-situ AFM images of Au(111) in  $O_2$  saturated 0.1 M  $LiPF_6$  in DMSO; (a) after flame annealing and before electrochemical treatment. Inset shows a phase image of typical herringbone reconstruction on Au(111); (b) after applying 2.05 V during 180 s.; (c) after 3.6 V during 180 s, (d) and 4.35 V during 180 s. Inset detail at larger magnification, and line profiles.

oxidized to dimethyl sulfone.<sup>28</sup> This may be due to the difficulty to oxidize large insulating  $Li_2O_2$  particles<sup>47</sup> or decomposition products of lithium peroxide in contact with the solvent and electrolyte.

On the other hand, detailed electrochemical FTIR studies failed to detect dimethyl sulfone in the liquid electrolyte adjacent to the electrode during ORR but at high anodic overpotentials, ca. over 4.3 V, during recharge DMSO was found to be electrochemically oxidized to dimethyl-sulfone.<sup>28</sup>

The gravimetric results with EQCM have been confirmed with AFM microscopic examination of the electrode surface after applying different potentials in DMSO- $LiPF_6$  electrolyte as shown in Figure 2. The Au electrode after a potential step in the ORR region at 2.05 V is covered by oxygen reduction products and line profiles of particles with 10–15 nm average height. After 60 s of oxidation at 4.35 V most of the deposit is converted into soluble products but nevertheless a thin layer of decomposition products cannot be removed. For longer times of  $Li_2O_2$  deposition, that is, 180 s. much thicker deposits (i.e., 40–50 nm) with similar texture to recent reports of large particles and flakes are apparent (see Supporting Information). These large lithium peroxide particles are formed from disproportion of lithium superoxide in the solution.<sup>24,42,48,49</sup> Unlike the deposits formed on Au, on HOPG, much less reactive surface, discrete particles mainly decorating steps have been found.<sup>31</sup>

A potential step from the open circuit potential of an Au electrode in  $O_2$  saturated 0.1 M  $LiPF_6$  in DMSO to 2.05 V was applied for 3 min recording the current. The integrated

cathodic charge in each case is shown in the respective legend of Figures 3–5. The respective chrono-amperometric ORR transients are depicted in Figure SI.

Figures 3, 4, and 5 depict the XPS results for three solvent–electrolyte pairs: DMSO/ $LiPF_6$ ; ACN/ $LiPF_6$ ; and ACN/ $LiBF_4$  before ORR (blank) and after polarization at 2.05, 3.35, and 4.55 V respectively. Spectroscopic C 1s, O 1s, Li 1s, F 1s, S 2p, and P 2p regions were analyzed. As shown in Figures 3–5 below, none of the studied elements O, Li, C, F, P, B, N, and S were present on the surfaces before exposure to the lithium electrolyte and subject to electrochemical experiments in the presence of molecular oxygen. Also, in the absence of oxygen in the electrolyte no electrochemical reaction was observed in the potential window studied<sup>10</sup> with the exception DMSO oxidation of to dimethyl sulfone on Au above 4.3 V.<sup>28</sup>

After oxygen reduction in lithium containing electrolyte at 2.05 V, all solvent–electrolyte systems show evidence of  $Li_2O_2$  formation with O 1s peak at 531.5 eV and Li 1s at 56 eV.<sup>16,50,51</sup>

The overlapping contribution of Au 5p photoelectrons in the binding energy region of the Li 1s was removed considering the Au attenuation factor.

Besides the expected signals for  $Li_2O_2$  on the surface in all systems studied, C 1s signals confirm the decomposition of DMSO in contact with the Au surface during the ORR since this is the only source of carbon. Peaks for C 1s at 290 eV and O 1s at 532.7 eV are characteristic of  $Li_2CO_3$ <sup>17,51</sup> and also C 1s peaks at 285 and 286 eV for other carbon containing species.<sup>51</sup> The 286 eV peak correspond to  $sp^3$  carbon from DMSO or its decomposition molecular products (see below). Furthermore, S

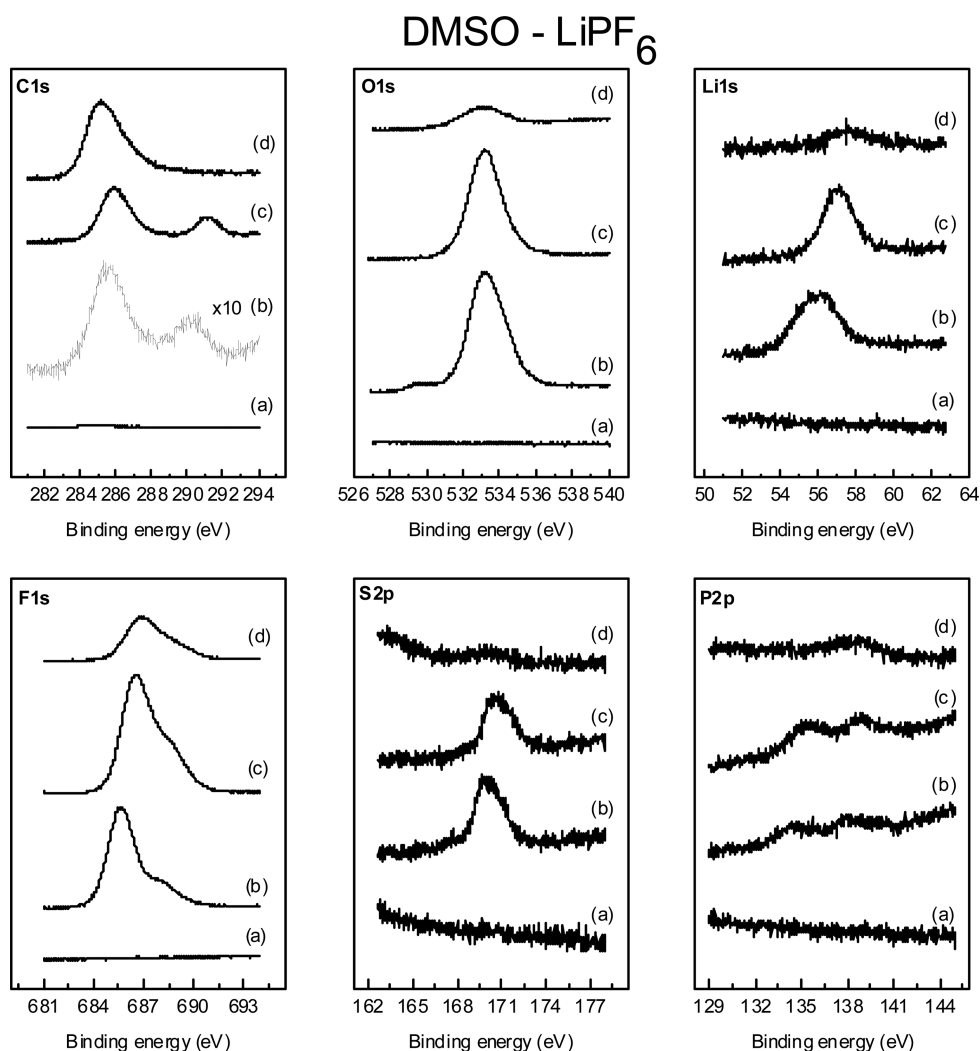


**Figure 3.** XPS spectra for O, Li, C, F, S, and P for the Au electrode after ORR in 0.1 M LiPF<sub>6</sub> in DMSO. (a) blank, (b) 2.05 V, (c) 3.35 V, and (d) 4.50 V.  $q = 6 \text{ mC}\cdot\text{cm}^{-2}$ .

2p broad peak at 170 eV also confirms the decomposition of DMSO.<sup>17</sup> Decomposition of the electrolyte anion PF<sub>6</sub><sup>-</sup> in contact with the oxygen reduction species at the Au surface is also apparent from the signals of F 1s with peaks at 685.5 and 687.8 eV for LiF and LiPF<sub>6</sub> or Li<sub>x</sub>PO<sub>y</sub>F<sub>x</sub><sup>51</sup> and also small peaks for P 2p at 134 and 137 eV.

The results in ACN/LiPF<sub>6</sub> are presented in Figure 4 and the main XPS features are O 1s peak at 534 and 535 eV; Li 1s at 58 eV, a broad C 1s peak at 287 eV, F 1s at 687 and 689 eV; P 2p at 137 and 141 eV but no N 1s peak was observed.

The third solvent–electrolyte pair studied was ACN with LiBF<sub>4</sub> and the surface products of the ORR resulted in XPS shown in Figure 5. A very broad O 1s peak at 533 with 3 eV width at half-maximum; Li 1s at 58 eV, a broad C 1s peak at 287 eV, F 1s at 687 and 689 eV; B 1s at 193 and 195 eV which correspond to B–O and B–F respectively.<sup>51</sup> No N 1s peak was observed at 400 eV region. Therefore, the decomposition of ACN does not yield insoluble nitrogen compounds on the surface.

The experimental evidence described above clearly demonstrates the instability of DMSO and ACN in contact with Li<sub>2</sub>O<sub>2</sub> deposited on Au. Since infrared absorption reflection spectroscopy (IRRAS) has shown that no appreciable dimethyl sulfone is formed in the liquid electrolyte,<sup>28</sup> we conclude that the

reaction of DMSO and ACN with Li<sub>2</sub>O<sub>2</sub> takes place at the solid/liquid interface producing an overlayer of decomposition products, mainly LiF, Li<sub>2</sub>CO<sub>3</sub>, ROR, ROOR, Li<sub>2</sub>SO<sub>4</sub>, etc. The surface to volume ratio is very high for XPS which examines only the topmost 2–5 nm overlayer of much thicker Li<sub>2</sub>O<sub>2</sub> deposits.

Electrochemical quartz crystal microbalance has shown, both in cyclic voltammetry and chronoamperometry, mass per electron (mpe) values (obtained from mass to charge plots) that largely exceed those values expected for simple O<sub>2</sub> to O<sub>2</sub>Li or Li<sub>2</sub>O<sub>2</sub> reactions eqs 1–4 and this led us to conclude that solvent or decomposition products codeposition simultaneous to the Li<sub>2</sub>O<sub>2</sub> and/or side reactions such as electrolyte degradation should be taken into consideration to explain the experimental evidence.<sup>52</sup> Co-deposition of dimethyl sulfoxide or dimethyl ion strongly coordinated to Li<sup>+</sup> ions forming ion pairs with superoxide anions, [Li<sup>+</sup>]<sub>DMSO</sub>O<sub>2</sub><sup>-</sup> and further disproportion to Li<sub>2</sub>O<sub>2</sub> would facilitate the heterogeneous reaction with DMSO and LiPF<sub>6</sub> with peroxide at the solid/liquid interface.

The quantitative analysis (see below) indicates less carbon species on the surface for the ORR from acetonitrile electrolyte but a substantial decomposition of PF<sub>6</sub><sup>-</sup> with formation of LiF as seen at 687e<sup>53</sup>

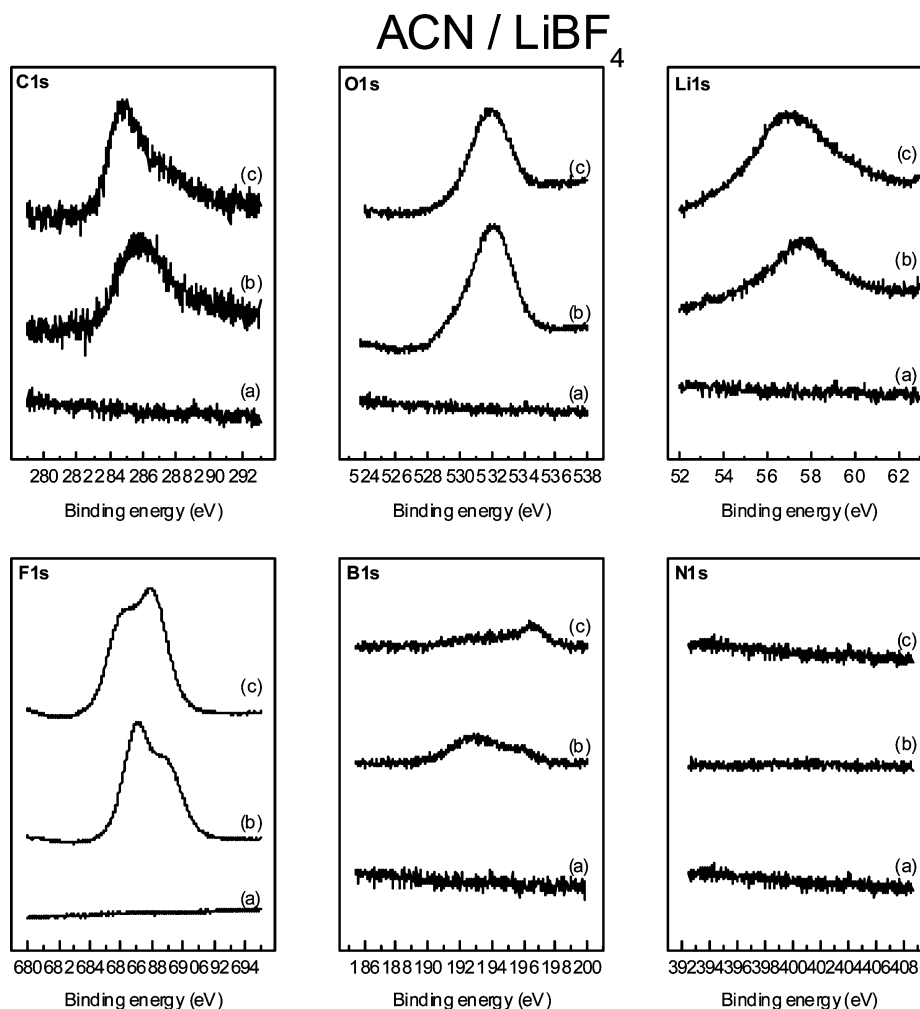


**Figure 5.** XPS spectra for O, Li, C, F, S, and P for the Au electrode after ORR in in 0.1 M LiBF<sub>4</sub> in CH<sub>3</sub>CN. (a) blank, (b) 2.05 V, c) 4.50 V.  $q = 9 \text{ mC}\cdot\text{cm}^{-2}$ .

The integrated XPS signals multiplied by an instrumental relative sensitivity factor, were computed for each element in each of the different electrolytes. The results for each electrolyte were normalized by the corresponding C 1s signal and are shown in Table I. Lithium, fluorine and oxygen are the main surface elements together with carbon.

With the assumption of Li<sup>+</sup> as the only cation present in the electrolyte the relative amounts of LiF and Li<sub>2</sub>CO<sub>3</sub> have been estimated from the XPS characteristic peaks of C 1s at 291 eV for carbonate and F 1s at 685.5 eV characteristic of fluoride and also the O 1s peak at 528.5 eV yielded a small amount of lithium oxide. Therefore, the major component at the surface examined by XPS which is only the 2 nm topmost layer of deposit is lithium fluoride from electrolyte degradation. The rest of components were calculated taking into account these results and the respective stoichiometry as shown in Table II. Other possible decomposition species are LiBxF<sub>y</sub>, B–P–O–R–R, ROOR, RH, ROR, LiOOR.

We further analyzed the total C 1s and F 1s XPS signals as markers for the instability of the solvent and electrolyte salt. Table III shows the relative amount of each element normalized.

Although the ORR only surface product in lithium containing electrolyte expected from eqs 1-4 is Li<sub>2</sub>O<sub>2</sub>, LiF appears to be the major surface component at the interface

between lithium peroxide and the liquid electrolyte from the decomposition of LiPF<sub>6</sub>.

During the oxidation cycle, the surface products formed during the ORR on Au start to oxidize above 2.96 V, the reversible potential for the O<sub>2</sub>/Li<sub>2</sub>O<sub>2</sub> reaction, with a steady state anodic current until solvent oxidation takes place at 4.2–4.3 V. At the onset of the surface oxidation, only a fraction of the deposit is removed from the surface (Figure 2C); and at 4.35 V only a molecular deposit remains on the surface (Figure 2D). At this extreme anodic potential the electrode can be recovered in the negative going sweep and the ORR voltammetry shows identical curves to the clean gold electrode while almost all the mass deposited during the ORR is lost at that potential as can be seen in Figure 1A.<sup>40</sup>

The gravimetric EQCM data shows a slow decrease in mass from 3.4 V (at the start of anodic current) to 4.3 V and a sharp drop to almost the original mass in the potential interval of net DMSO electrochemical oxidation at slow scan rate (2 mV·s<sup>-1</sup>).

Figures 3–5 depict the C 1s, O 1s, F 1s, Li 1s, P 2p, and S 2p XPS signals at potentials during reoxidation of ORR products on the Au surface. For DMSO–LiPF<sub>6</sub> an increase in C 1s and F 1s is observed while O 1s does not increase appreciably but the Li 1s peak shifts to higher binding energy as S 2p does. It should be noted the effect of contact time between the solid Li<sub>2</sub>O<sub>2</sub> and the liquid electrolyte which results in larger amount

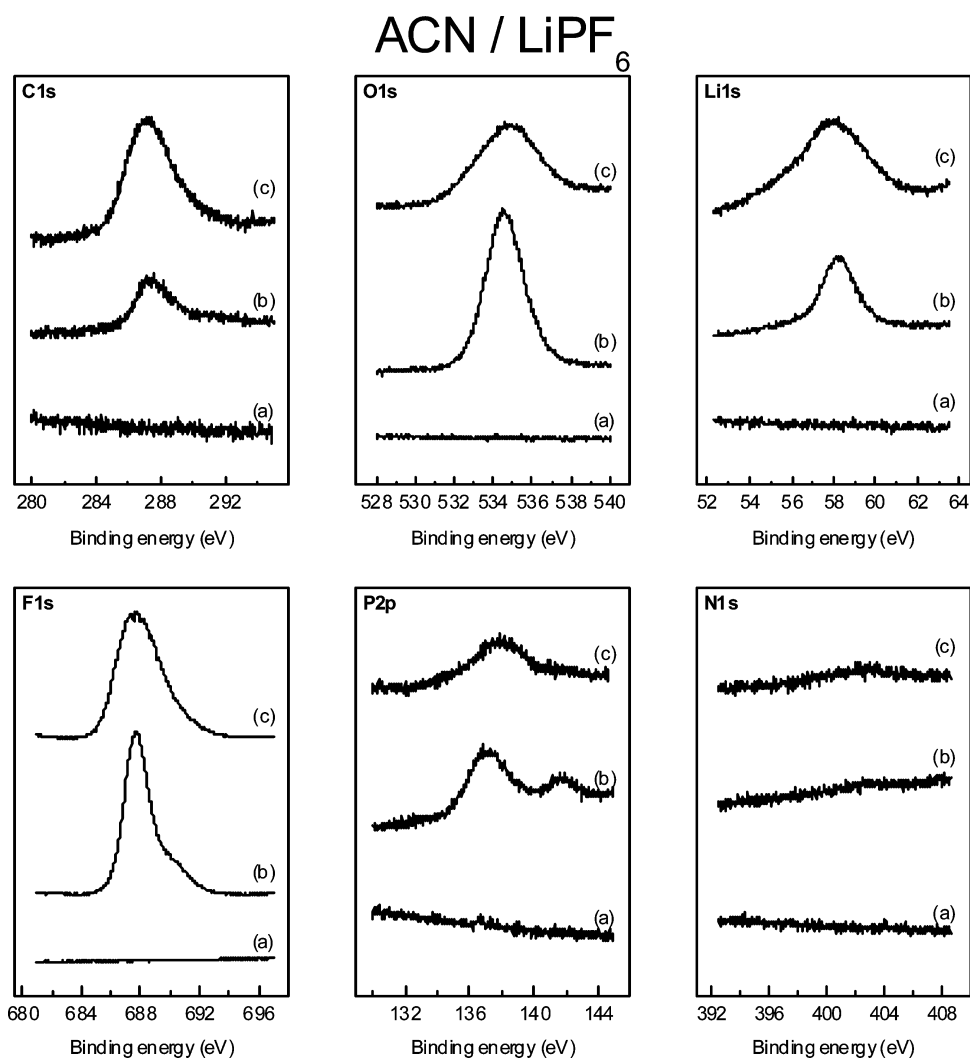


**Figure 4.** XPS spectra for O, Li, C, F, S, and P for the Au electrode after ORR in 0.1 M LiPF<sub>6</sub> in CH<sub>3</sub>CN. (a) blank, (b) 2.05 V, (c) 4.50 V.  $q = 9 \text{ mC}\cdot\text{cm}^{-2}$ .

**Table I.** Integrated XPS Signals Normalized to C 1s Peak for the Elements Analyzed in the Solvent/Electrolyte Pairs DMSO/LiPF<sub>6</sub>; CH<sub>3</sub>CN/LiPF<sub>6</sub> and LiBF<sub>4</sub>/CH<sub>3</sub>CN for ORR at 2.05 V

electrolyte	C 1s	O 1s	S 2p	Li 1s	F 1s	P 2p	N 1s	B 1s
LiPF <sub>6</sub> /DMSO	1.0	3.9	0.3	4.4	3.0	0.3		
LiPF <sub>6</sub> /CH <sub>3</sub> CN	1.0	3.3		13.9	12.4	1.1	0	
LiBF <sub>4</sub> /CH <sub>3</sub> CN	1.0	1.4		4.9	4.0		0	2.3

**Table II.** Estimated Percentage of the Different Surface Components from XPS Analysis for ORR at 2.05 V

electrolyte	Li <sub>2</sub> CO <sub>3</sub>	LiF	Li <sub>2</sub> O <sub>2</sub>	Li <sub>2</sub> SO <sub>4</sub>	others
LiPF <sub>6</sub> /DMSO	5.6	62.1	6.7	7.8	17.8
LiPF <sub>6</sub> /CH <sub>3</sub> CN	0.8	79.3	12.0		7.9
LiBF <sub>4</sub> /CH <sub>3</sub> CN	0	51.5	13.0		35.5

of decomposition products observed in Figure 3b. The Li 1s peak seen at 56, 1 eV for 2.05 V shifts to 57.1 eV at 3.35 V and the S 2p peak also shifts less than 1 eV to larger binding energies. These shifts are due to increase in LiF at the surface and oxidation of sulfur containing species. Also, some P 2p and

**Table III.** C 1s and F 1s XPS Integrated Signals As Markers of Solvent and Salt Instability for ORR at 2.05 V

	C 1s	F 1s
LiPF <sub>6</sub> /DMSO	1.9	1.5
LiPF <sub>6</sub> /CH <sub>3</sub> CN	1.1	3.0
LiBF <sub>4</sub> /CH <sub>3</sub> CN	1.0	1.0

increase in the F 1s peak confirm decomposition of the electrolyte PF<sub>6</sub><sup>-</sup> at the oxidation onset.

At high overpotential for DMSO-LiPF<sub>6</sub> pair the oxygen O 1s peak at 532 eV decreases and the C 1s peak the 290 eV characteristic of lithium carbonate disappears while the 285 eV is apparent with increase in the P 2p signal. For the ACN/LiBF<sub>4</sub> solvent electrolyte pair there is no evidence of N 1s so that no nitrogen surface compounds were found, but small B 1s peak and two peaks for F 1s show partial reaction of the electrolyte.

Differential electrochemical mass spectrometry (DEMS) simultaneous to the ORR in LiPF<sub>6</sub>/DMSO at 2.0 V has shown that only a small fraction of the O<sub>2</sub> consumed during oxygen reduction to Li<sub>2</sub>O<sub>2</sub> is evolved at 3.5 V as detected by the mass 32 ionic current during oxidation (see Figure 6) in good agreement with recent similar Au gas diffusion electrodes

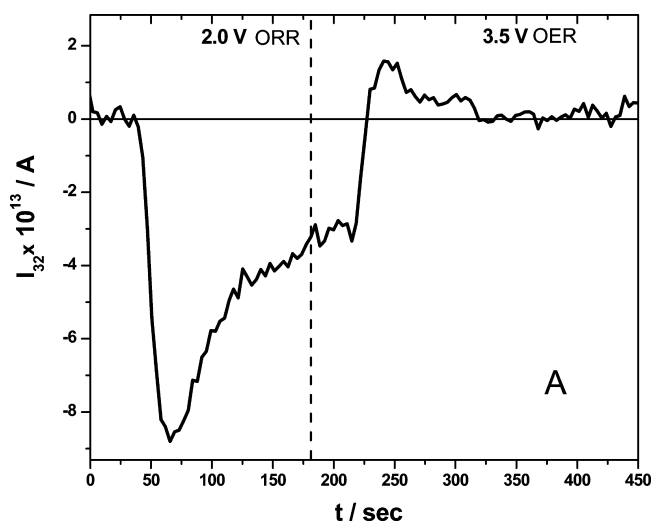


**Figure 6.** DEMS ionic current for mass 32 during ORR in 0.1 M LiPF<sub>6</sub> DMSO solution O<sub>2</sub> saturated at 2.0 and 3.6 V, flow rate 2.3 mL/min, baseline corrected.

reported by Bondue et al.<sup>15</sup> These results are consistent with partial degradation of solvent and LiPF<sub>6</sub> electrolyte reported here by XPS, AFM, and gravimetric evidence.

During surface oxidation at extreme potentials with almost total mass recovery (Figure 2) DEMS results depicted in Figure 7 for masses 44 and 32 ionic currents demonstrate that CO<sub>2</sub> is

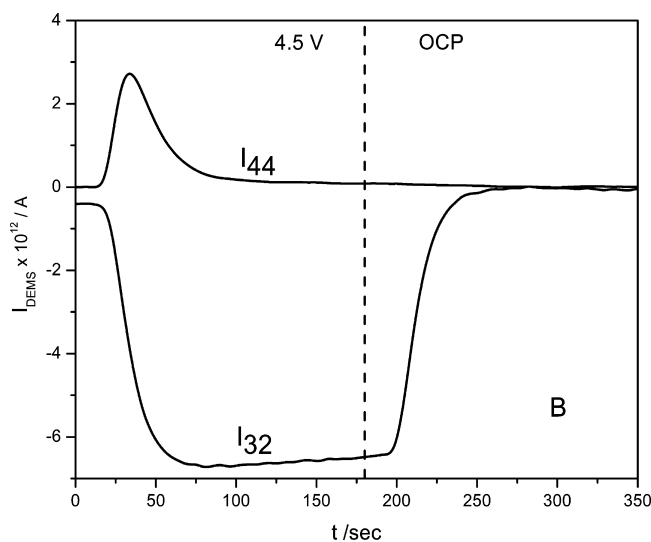


**Figure 7.** DEMS ionic current for masses 32 and 44 during ORR in 0.1 M LiPF<sub>6</sub> O<sub>2</sub> saturated DMSO solution at 2.0 and 3.6 V, flow rate 2.3 mL/min during oxidation at 4.5 V and open circuit potential after oxidation (OCP).

evolved and oxygen concentration depleted at the porous Au sputtered membrane electrode in a chronoamperometry at 4.5 V. Then at open circuit potential (OCP) mass 44 ionic current for CO<sub>2</sub> drops to zero and mass 32 ionic current recovers to the basal level. These results are consistent with XPS disappearance of C 1s at 290 eV due to carbonate species and oxidation of DMSO consuming O<sub>2</sub> as predicted by the mechanism proposed by Aurbach et al. for the oxidation of DMSO.<sup>18</sup>

Unlike the studies with full batteries, low surface area Au electrodes and high surface sensitivity methods used in the

present study have allowed us to get an insight into the surface chemistry of ORR highly reactive intermediates and their reactivity toward solvent and electrolyte.

Furthermore, formation of large insulating lithium peroxide particles from a solution phase mechanism and formation of spurious material by reaction of solvent and electrolyte with surface oxidant species contributes to the capacity fading of lithium air battery cathodes.

## CONCLUSIONS

The O<sub>2</sub>/Li<sub>2</sub>O<sub>2</sub> electrode reaction has been studied on low surface area Au electrodes in three solvent–electrolyte pairs (0.1 M LiPF<sub>6</sub>/DMSO, LiPF<sub>6</sub>/ACN and LiBF<sub>4</sub>/ACN) using an electrochemical cell coupled to UHV XPS spectrometer and complemented by other techniques (EQCM, AFM, and DEMS).

The XPS spectra of the surfaces after treatment at selected electrode potentials for the O<sub>2</sub> reduction and reoxidation of the surface show the presence of C 1s and S 2p from solvent decomposition and of F 1s and P 2p from electrolyte decomposition. It is suggested that the outermost surface of Li<sub>2</sub>O<sub>2</sub> deposit react with the solvents and electrolytes to form a thin layer of side products. ACN results in less solvent decomposition than DMSO and LiBF<sub>4</sub> results in less electrolyte decomposition than LiPF<sub>6</sub>. The RRDE and EQCM results with low donor number acetonitrile have shown that soluble superoxide cannot be detected in solution given the poor solvation of ACN for Li<sup>+</sup> ion and the ORR proceeds by the surface mechanism since the deposited mass grows linearly with time (charge) in galvanostatic pulses from the beginning of the ORR pulse with a slope that corresponds to mpe of 23 g per Faraday in repetitive pulses.<sup>52</sup>

XPS Li 1s and O 1s peaks due to Li<sub>2</sub>O<sub>2</sub> and decomposition products such as carbonate, organics, LiF, high oxidation sulfur and phosphorus compounds were observed. All the experimental evidence with high sensitive surface to volume ratio such as XPS, AFM, and EQCM show that O<sub>2</sub> reduction products can only be removed at very high overpotentials. DEMS experiments confirmed evolution of CO<sub>2</sub> and consumption of O<sub>2</sub> at 4.5 V in agreement with XPS evidence of carbonate surface removal, but LiF could not be removed completely in a round trip of the Li–O<sub>2</sub> battery cathode as confirmed by AFM and EQCM.

## ASSOCIATED CONTENT

### Supporting Information

The Supporting Information is available free of charge on the ACS Publications website at DOI: 10.1021/acs.langmuir.5b02130.

XPS experimental setup, Figures S1–S7 (PDF)

## AUTHOR INFORMATION

### Corresponding Author

\*E-mail: calvo@qi.fcen.uba.ar.

### Notes

The authors declare no competing financial interest.

## ACKNOWLEDGMENTS

Funding from CONICET and ANPCyT PICT 2012 No. 1452 and FS-Nano 07 and research doctoral and postdoctoral fellowships from CONICET by F.M., W.R.T., and A.Y.T. are gratefully acknowledged.

## REFERENCES

- (1) Abraham, K. M.; Lithium–air and other batteries beyond lithium-ion batteries. In *Lithium Batteries: Advanced Technologies and Applications*, 1st ed.; Bruno Scrosati, K. M. A., van Schalkwijk, W., Hassoun, J., Eds.; John Wiley & Sons, Inc, 2013.
- (2) Bruce, P. G.; Freunberger, S. A.; Hardwick, L. J.; Tarascon, J.-M. Li–O<sub>2</sub> and Li–S batteries with high energy storage. *Nat. Mater.* **2011**, *11* (1), 19.
- (3) Christensen, J.; Albertus, P.; Sanchez-Carrera, R. S.; Lohmann, T.; Kozinsky, B.; Liedtke, R.; Ahmed, J.; Kojic, A. A Critical Review of Li/Air Batteries. *J. Electrochem. Soc.* **2012**, *159* (2), R1–R30.
- (4) Freunberger, S. A.; Chen, Y.; Drewett, N. E.; Hardwick, L. J.; Barde, F.; Bruce, P. G. The Lithium–Oxygen Battery with Ether-Based Electrolytes. *Angew. Chem., Int. Ed.* **2011**, *50* (37), 8609–8613.
- (5) Hardwick, L. J.; Bruce, P. G. The pursuit of rechargeable non-aqueous lithium–oxygen battery cathodes *Current Opinion in Solid State & Curr. Opin. Solid State Mater. Sci.* **2012**, *16* (4), 178–185.
- (6) Abraham, K. M.; Jiang, Z. A polymer electrolyte-based rechargeable lithium/oxygen battery. *J. Electrochem. Soc.* **1996**, *143* (1), 1–5.
- (7) Ogasawara, T.; Debart, A.; Holzapfel, M.; Novak, P.; Bruce, P. G. Rechargeable Li<sub>2</sub>O<sub>2</sub> electrode for lithium batteries. *J. Am. Chem. Soc.* **2006**, *128* (4), 1390–1393.
- (8) Laoire, C. O.; Mukerjee, S.; Abraham, K. M.; Plichta, E. J.; Hendrickson, M. A. *J. Phys. Chem. C* **2010**, *114* (19), 9178–9186.
- (9) Xu, D.; Wang, Z.-l.; Xu, J.-j.; Zhang, L.-l.; Zhang, X.-b. Novel DMSO-based electrolyte for high performance rechargeable Li–O<sub>2</sub> batteries. *Chem. Commun.* **2012**, *48* (55), 6948–6950.
- (10) Trahan, M. J.; Mukerjee, S.; Plichta, E. J.; Hendrickson, M. A.; Abraham, K. M. Studies of Li–Air Cells Utilizing Dimethyl Sulfoxide-Based Electrolyte. *J. Electrochem. Soc.* **2012**, *160* (2), A259–A267.
- (11) McCloskey, B. D.; Valery, A.; Luntz, A. C.; Gowda, S. R.; Wallraff, G. M.; Garcia, J. M.; Mori, T.; Krupp, L. E. Combining Accurate O<sub>2</sub> and Li<sub>2</sub>O<sub>2</sub> Assays to Separate Discharge and Charge Stability Limitations in Nonaqueous Li–O<sub>2</sub> Batteries. *J. Phys. Chem. Lett.* **2013**, *4* (17), 2989–2993.
- (12) Younesi, R.; Hahlin, M.; Bjorefors, F.; Johansson, P.; Edstrom, K. Li–O<sub>2</sub> Battery Degradation by Lithium Peroxide (Li<sub>2</sub>O<sub>2</sub>): A Model Study. *Chem. Mater.* **2013**, *25* (1), 77–84.
- (13) McCloskey, B. D.; Bethune, D. S.; Shelby, R. M.; Mori, T.; Scheffler, R.; Speidel, A.; Sherwood, M.; Luntz, A. C. Limitations in Rechargeability of Li–O<sub>2</sub> Batteries and Possible Origins. *J. Phys. Chem. Lett.* **2012**, *3* (20), 3043–3047.
- (14) McCloskey, B. D.; Scheffler, R.; Speidel, A.; Girishkumar, G.; Luntz, A. C. On the Mechanism of Nonaqueous Li–O<sub>2</sub> Electrochemistry on C and Its Kinetic Overpotentials: Some Implications for Li–Air Batteries. *J. Phys. Chem. C* **2012**, *116* (45), 23897–23905.
- (15) Bondue, C. J.; Abd-El-Latif, A. A.; Hegemann, P.; Baltruschat, H. Quantitative Study for Oxygen Reduction and Evolution in Aprotic Organic Electrolytes at Gas Diffusion Electrodes by DEMS. *J. Electrochem. Soc.* **2015**, *162* (3), A479–A487.
- (16) Younesi, R.; Norby, P.; Vegge, T. A New Look at the Stability of Dimethyl Sulfoxide and Acetonitrile in Li–O<sub>2</sub> Batteries. *ECS Electrochem. Lett.* **2014**, *3* (3), A15–A18.
- (17) Chalasani, D.; Lucht, B. L. Reactivity of Electrolytes for Lithium–Oxygen Batteries with Li<sub>2</sub>O<sub>2</sub>. *ECS Electrochem. Lett.* **2012**, *1* (2), A38–A42.
- (18) Sharon, D.; Afri, M.; Noked, M.; Garsuch, A.; Frimer, A. A.; Aurbach, D. Oxidation of dimethyl sulfoxide solutions by electrochemical reduction of oxygen. *J. Phys. Chem. Lett.* **2013**, *4* (18), 3115–3119.
- (19) Torres, W.; Mozhuzhukhina, N.; Tesio, A. Y.; Calvo, E. J. A rotating ring disk electrode study of the oxygen reduction reaction in lithium containing dimethyl sulfoxide electrolyte: Role of Superoxide. *J. Electrochem. Soc.* **2014**, *161* (14), A2204–A2209.
- (20) Torres, W. R.; Cantoni, L.; Tesio, A. Y.; Del Pozo Vazquez, M.; Calvo, E. J. EQCM Study of the oxygen reduction on Au electrode in DMSO and Acetonitrile with LiPF<sub>6</sub>. *J. Electroanal. Chem.* **2014**, submitted.
- (21) Torres, W. R.; Tesio, A. Y.; Calvo, E. J. Solvent co-deposition during oxygen reduction on Au in DMSO LiPF<sub>6</sub>. *Electrochem. Commun.* **2014**, *49*, 38.
- (22) Adams, B. D.; Radtke, C.; Black, R.; Trudeau, M. L.; Zaghbi, K.; Nazar, L. F. Current density dependence of peroxide formation in the Li–O<sub>2</sub> battery and its effect on charge. *Energy Environ. Sci.* **2013**, *6* (6), 1772–1778.
- (23) Aetukuri, N. B.; McCloskey, B. D.; Garcia, J. M.; Krupp, L. E.; Viswanathan, V.; Luntz, A. C. Solvating additives drive solution-mediated electrochemistry and enhance toroid growth in non-aqueous Li–O<sub>2</sub> batteries. *Nat. Chem.* **2014**, *7* (1), 50–56.
- (24) Johnson, L.; Li, C.; Liu, Z.; Chen, Y.; Freunberger, S. A.; Ashok, P. C.; Praveen, B. B.; Dholakia, K.; Tarascon, J.-M.; Bruce, P. G. The role of LiO<sub>2</sub> solubility in O<sub>2</sub> reduction in aprotic solvents and its consequences for Li–O<sub>2</sub> batteries (vol 6, pg 1091, 2014). *Nat. Chem.* **2014**, *7* (1), 87–87.
- (25) Mitchell, R. R.; Gallant, B. M.; Shao-Horn, Y.; Thompson, C. V. Mechanisms of Morphological Evolution of Li<sub>2</sub>O<sub>2</sub> Particles during Electrochemical Growth. *J. Phys. Chem. Lett.* **2013**, *4* (7), 1060–1064.
- (26) Safari, M.; Adams, B. D.; Nazar, L. F. Kinetics of Oxygen Reduction in Aprotic Li–O<sub>2</sub> Cells: A Model-Based Study. *J. Phys. Chem. Lett.* **2014**, *5* (20), 3486–3491.
- (27) Kwabi, D. G.; Batcho, T. P.; Amanchukwu, C. V.; Ortiz-Vitoriano, N.; Hammond, P.; Thompson, C. V.; Shao-Horn, Y. Chemical instability of dimethyl sulfoxide in lithium-air batteries. *J. Phys. Chem. Lett.* **2014**, *5* (16), 2850–2856.
- (28) Mozhuzhukhina, N.; Mendez De Leo, L. P.; Calvo, E. J. Infrared Spectroscopy Studies on Stability of Dimethyl Sulfoxide for Application in a Li–Air Battery. *J. Phys. Chem. C* **2013**, *117* (36), 18375–18380.
- (29) Mendez De Leo, L. P.; de la Llave, E.; Scherlis, D.; Williams, F. J. Molecular and electronic structure of electroactive self-assembled monolayers. *J. Chem. Phys.* **2013**, *138* (11), 114707–114707.
- (30) Tarascon, J. M.; Guyomard, D. Li metal-free rechargeable batteries based on Li<sub>1+x</sub>Mn<sub>2</sub>O<sub>4</sub> cathodes (0 ≤ x ≤ 1) and carbon anodes. *J. Electrochem. Soc.* **1991**, *138* (10), 2864–2868.
- (31) Herrera, S. E.; Tesio, A. Y.; Clarenc, R.; Calvo, E. J. AFM Study of Oxygen Reduction Products on HOPG in LiPF<sub>6</sub> DMSO Electrolyte. *J. Phys. Chem. Phys.* **2014**, *16* (21), 9925.
- (32) Calvo, E. J.; Etchenique, R.; Bartlett, P. N.; Singhal, K.; Santamaria, C. Quartz crystal impedance studies at 10 MHz of viscoelastic liquids and films. *Faraday Discuss.* **1997**, *107*, 141–157.
- (33) H, B. Differential Electrochemical Mass Spectrometry. *J. Am. Soc. Mass Spectrom.* **2004**, *15*, 1693–1706.
- (34) Baltruschat, H.; El Aziz, A.; El-Latif, A. Electrochemical Mass Spectroscopy. In *Encyclopedia of Applied Electrochemistry*; Kreysa, G., Ota, K.-i., Savinell, R., Eds.; Springer: New York, 2014; pp 507–516.
- (35) Abd-El-Latif, A. A.; Bondue, C. J.; Ernst, S.; Hegemann, M.; Kaul, J. K.; Khodayari, E.; Mostafa, K.; Stefanova, A.; Baltruschat, H. Insights into electrochemical reactions by differential electrochemical mass spectroscopy. *TrAC, Trends Anal. Chem.* **2015**, *70*, 4.
- (36) Ashton, S. J. *Design, Construction and Research Application of a Differential Electrochemical Mass Spectrometer (DEMS)*; Technical University of Munich: Germany, Munich, 2011.
- (37) Hossain, M. S.; Tryk, D.; Yeager, E. The electrochemistry of graphite and modified graphite surfaces: the reduction of O<sub>2</sub>. *Electrochim. Acta* **1989**, *34* (12), 1733–1737.
- (38) Laoire, C. O.; Mukerjee, S.; Abraham, K. M.; Plichta, E. J.; Hendrickson, M. A. Elucidating the Mechanism of Oxygen Reduction for Lithium–Air Battery Applications. *J. Phys. Chem. C* **2009**, *113* (46), 20127–20134.
- (39) Laoire, C. O.; Mukerjee, S.; Abraham, K. M.; Plichta, E. J.; Hendrickson, M. A. Influence of Nonaqueous Solvents on the Electrochemistry of Oxygen in the Rechargeable Lithium–Air Battery. *J. Phys. Chem. C* **2010**, *114* (19), 9178–9186.
- (40) Torres, W.; Mozhuzhukhina, N.; Tesio, A. Y.; Calvo, E. J. A Rotating Ring Disk Electrode Study of the Oxygen Reduction Reaction in Lithium Containing Dimethyl Sulfoxide Electrolyte. *J. Electrochem. Soc.* **2014**, *161* (14), A2204–A2209.

(41) Xue, K.-H.; McTurk, E.; Johnson, L.; Bruce, P. G.; Franco, A. A. A Comprehensive Model for Non-Aqueous Lithium Air Batteries Involving Different Reaction Mechanisms. *J. Electrochem. Soc.* **2015**, *162* (4), A614–A621.

(42) Aetukuri, N. B.; McCloskey, B. D.; Garcia, J. M.; Krupp, L. E.; Viswanathan, V.; Luntz, A. C. Solvating additives drive solution-mediated electrochemistry and enhance toroid growth in non-aqueous Li-O<sub>2</sub> batteries. *Nat. Chem.* **2014**, *7* (1), 50–56.

(43) Laoire, C. O.; Mukerjee, S.; Plichta, E. J.; Hendrickson, M. A.; Abraham, K. M. Studies of Li-Air Cells Utilizing Dimethyl Sulfoxide-Based Electrolyte. *J. Electrochem. Soc.* **2011**, *158* (3), A302–A308.

(44) Yu, Q.; Ye, S. In Situ Study of Oxygen Reduction in Dimethyl Sulfoxide (DMSO) Solution: A Fundamental Study for Development of the Lithium–Oxygen Battery. *J. Phys. Chem. C* **2015**, *119* (22), 12236–12250.

(45) Torres, W. R.; Cantoni, L.; Tesio, A. Y.; Del Pozo, M.; Calvo, E. J. EQCM Study of Oxygen Cathodes in DMSO LiPF<sub>6</sub> Electrolyte. *J. Electroanal. Chem.* **2015**, submitted.

(46) Mozshukhina, N.; Semino, R.; Zaldivar, G.; Lariaa, D. H.; Calvo, E. J. Preferential solvation of lithium ions in acetonitrile-DMSO mixtures. **2013**. In preparation.

(47) Meini, S.; Solchenbach, S.; Piana, M.; Gasteiger, H. A. The Role of Electrolyte Solvent Stability and Electrolyte Impurities in the Electrooxidation of Li<sub>2</sub>O<sub>2</sub> in Li–O<sub>2</sub> Batteries. *J. Electrochem. Soc.* **2014**, *161* (9), A1306–A1314.

(48) Gallant, B. M.; Kwabi, D. G.; Mitchell, R. R.; Zhou, J.; Thompson, C. V.; Shao-Horn, Y. Influence of Li<sub>2</sub>O<sub>2</sub> morphology on oxygen reduction and evolution kinetics in Li–O<sub>2</sub> batteries. *Energy Environ. Sci.* **2013**, *6* (8), 2518–2528.

(49) Gallant, B. M.; Mitchell, R. R.; Kwabi, D. G.; Zhou, J.; Zuin, L.; Thompson, C. V.; Shao-Horn, Y. Chemical and Morphological Changes of Li–O<sub>2</sub> Battery Electrodes upon Cycling. *J. Phys. Chem. C* **2012**, *116* (39), 20800–20805.

(50) Lu, Y.-C.; Crumlin, E. J.; Veith, G. M.; Harding, J. R.; Mutoro, E.; Baggetto, L.; Dudney, N. J.; Liu, Z.; Shao-Horn, Y. *In Situ Ambient Pressure X-ray Photoelectron Spectroscopy Studies of Lithium-Oxygen Redox Reactions*, Scientific Reports 2.

(51) Yao, K. P. C.; Kwabi, D. G.; Quinlan, R. A.; Mansour, A. N.; Grimaud, A.; Lee, Y.-L.; Lu, Y.-C.; Shao-Horn, Y. Thermal Stability of Li<sub>2</sub>O<sub>2</sub> and Li<sub>2</sub>O for Li-Air Batteries: In Situ XRD and XPS Studies. *J. Electrochem. Soc.* **2013**, *160* (6), A824–A831.

(52) Torres, W. R.; Cantoni, L.; Tesio, A. Y.; Del Pozo Vazquez, M.; Calvo, E. J. EQCM Study of the oxygen cathodes in DMSO LiPF<sub>6</sub> Electrolyte. *J. Electroanal. Chem.* **2015**, accepted.

(53) Lu, Y. C.; Kwabi, D. G.; Yao, K. P. C.; Harding, J. R.; Zhou, J.; Zuin, L.; Shao-Horn, Y. The discharge rate capability of rechargeable Li–O<sub>2</sub> batteries. *Energy Environ. Sci.* **2011**, *4* (8), 2999–3007.